Supporting Information for "Acceleration of warming, deoxygenation and acidification in the Arabian Gulf driven by weakening of summer winds"

Z. Lachkar[1], M. Mehari[1,*], F. Paparella[1], J. A. Burt[1,2]

[1]Mubadala Arabian Center for Climate and Environmental Sciences, New York University Abu Dhabi, Abu Dhabi, United Arab Emirates

[2]Water Research Center, New York University Abu Dhabi, Abu Dhabi, United Arab Emirates

*Now at: Global Modeling and Assimilation Office, Science Applications International Corporation, National Aeronautics and Space Administration Goddard Space Flight Center, Greenbelt, MD, USA

Contents of this file

1. Text S1: description of the model setup

The circulation model is based on the Regional Ocean Modeling System (ROMS) (Shchepetkin & McWilliams, 2005). Advection is formulated using a rotated-split third-

order upstream biased operator as described by Marchesiello, Debreu, and Couvelard (2009), while vertical mixing is represented using the non-local K-profile parameterization (KPP) scheme proposed by Large, McWilliams, and Doney (1994). The model's domain spans the Indian Ocean from 31.5°S to 31°N and 30°E to 120°E, with a horizontal resolution of 1/10° and 32 sigma-coordinate vertical layers, featuring enhanced resolution near the surface. Biogeochemical processes are simulated using a nitrogen-based nutrient, phytoplankton, zooplankton, detritus (NPZD) model, comprising two nutrient components (nitrate and ammonium), one phytoplankton, one zooplankton, and two detrital classes (Gruber et al., 2006). Previous observations highlight nitrogen as the primary limiting nutrient in the Gulf, justifying the adoption of a nitrogen-based NPZD model to explore Gulf biogeochemistry dynamics (Quigg et al., 2013; Al-Said et al., 2018; Al-Yamani & Naqvi, 2019). Furthermore, the model incorporates a module describing the oxygen cycle (Lachkar et al., 2021). At suboxic oxygen concentrations ($O_2 < 4$ mmol m^{-3}) nitrification halts, and the remineralization rate is reduced by half. Additionally, aerobic remineralization of detritus is replaced by water column denitrification, where nitrate substitutes oxygen as the electron acceptor. Benthic denitrification is also accounted for in the model, following the parameterization by (Middelburg et al., 1996). Additional details regarding the implementation of denitrification in the model are provided in Lachkar, Smith, Lévy, and Pauluis (2016). The model incorporates a carbon module comprising three state variables: dissolved inorganic carbon (DIC), total alkalinity (TA), and calcium carbonate (Lachkar & Gruber, 2013; Lachkar, 2014; de Verneil et al., 2022). Organic carbon is linked to organic nitrogen through the Redfield ratio of 106:16. Surface fluxes of

DIC and TA, propelled by variations in sea surface salinity, are included as virtual fluxes that scale proportionally with the sea surface salinity forcing. Carbonate chemistry is computed using routines from the Ocean Carbon-Cycle Model Intercomparison Project (OCMIP) (Orr et al., 2005). The formulation of air-sea gas transfer adopts a quadratic wind speed dependence as delineated by Wanninkhof (1992). Comprehensive details of the biogeochemical model are provided in Lachkar et al. (2021); de Verneil et al. (2022).

The hindcast simulation is forced by ECMWF ERA-Interim 6-hourly heat fluxes, air temperature, pressure, humidity, precipitation, and winds spanning the period from January 1980 to December 2018. Initial and lateral boundary conditions for temperature, salinity, currents, and sea surface height are derived from the ECMWF Ocean Reanalysis System 5 (ORAS5; Zuo et al., 2019). Nitrate and oxygen initial and lateral boundary conditions are based on World Ocean Atlas 2018 (Garcia et al., 2019). Initial and lateral boundary conditions for DIC and TA are obtained from GLODAP version 2 (Lauvset et al., 2016). Atmospheric pCO_2 is prescribed using monthly data from Mauna Loa (Keeling et al., 2005), while atmospheric CO_2 data preceding 1958 is extracted from Joos and Spahni (2008). Riverine inputs include nutrients (Krishna et al., 2016; Ramesh et al., 1995) but exclude carbon or alkalinity. To accommodate the accumulation of anthropogenic carbon at the open lateral boundaries during the simulation period, decadally-varying DIC is utilized, derived from available estimates of anthropogenic CO_2 (Key et al., 2004; Gruber et al., 2019; Olsen et al., 2019) regressed against atmospheric CO_2 concentrations. Initial and boundary conditions for DIC and TA are processed in accordance with de Verneil et al. (2022) to incorporate a seasonal cycle in the upper ocean.

The model is first spun up for an initial 30 years with a repeated normal year (neutral with respect to major climate variability modes; 1984) forcing for heat, freshwater and momentum fluxes but with increasing atmospheric CO_2 concentrations and DIC at the atmospheric and lateral boundaries (to represent the increasing carbon levels in the atmosphere and the ocean between 1950 and 1979) and is then run for a complete 39-year (1980-2018) forcing cycle where both atmospheric physical fluxes as well as carbon vary annually following observations (i.e., the total duration of the spin-up phase is 69 years). Following the spin-up phase, the model undergoes an additional forcing cycle, constituting the hindcast run (HR) used for analysis. This is similar to the forcing protocol used in the the CORE-II simulations and the Ocean Model Intercomparison Project (Griffies et al., 2016). Adhering to the recommendations of the RECCAP2 protocol, the spin-up run (characterized by climatological forcing and increasing CO_2) is extended to cover the same period (1980-2018) as the HR. This simulation, termed Constant Climate (CC hereafter), serves to quantify any artificial trends in circulation and biogeochemistry solely induced by model drift and contrasts them with trends estimated in the HR. Furthermore, this simulation is employed to disentangle ocean acidification driven by rising anthropogenic CO_2 in the atmosphere from changes induced by alterations in climate, ocean circulation, and biology.

2. Text S2: evaluation of model drift

To assess the potential impact of model drift on our findings, we examined the trends in several key variables within the CC simulation and compared them with those in the HR simulation. Given that all forcing, except CO_2, is climatological in CC, any long-term

changes in variables other than CO_2 and associated variables (e.g., pH) within CC can be attributed to artificial trends stemming from model drift. Conversely, trends in CO_2 (and associated variables such as pH) in CC primarily result from the increasing anthropogenic CO_2 levels in the atmosphere. Contrasting these trends with those in HR enables us to gauge the influence of climate change and variability on carbon dynamics in the region. Table S1 presents the trends (1980-2018) in averaged physical (e.g., temperature, salinity, density, Gulf outflow) and biogeochemical (e.g., nitrogen transport through the Strait, net primary productivity, oxygen, and pH) properties in the AG from both simulations. This comparison highlights that the trends observed in CC are typically 1 to 3 orders of magnitude smaller than those in the HR simulation for all variables except pH. This suggests that model drift is negligible in the focus area and that the identified trends in the HR runs are primarily driven by changes in regional climatic conditions.

3. Text S3: evaluation of the model

The model effectively replicates the observed distributions of sea surface temperature (SST) obtained from NOAA Optimum Interpolation Sea Surface temperature (OISST) data, which combines satellite and in-situ (ships and buoys) measurements, during both winter and summer seasons (see Fig S1). Notably, the model accurately captures the pronounced temperature gradients present across the AG between its northwestern and southeastern regions as well as the temperature progression from winter to summer in the SOO. This favorable agreement for SST is somewhat anticipated, given that the model's simulated surface temperature is constrained by AVHRR satellite observations though restoring of surface temperature. To assess the model's performance in reproducing the

three-dimensional structure of temperature and salinity within the region, we contrast our simulation with the limited historical observations available in the World Ocean Database (WOD) 2018 to bolster confidence in the simulated hydrography of the AG and the SOO.

For this purpose, we binned WOD observations monthly and on a 0.5x0.5 regular grid and regridded the model onto the same common grid. This comparison reveals that the model exhibits a similar range of variation in both temperature and salinity as depicted in the observations (see Fig S2 and Fig S3). Additionally, in both the AG and the SOO, modeled temperatures exhibit high correlations with WOD observations (R2 ranging between 0.84 in the SOO and 0.88 in the AG) and demonstrate limited systematic biases. Furthermore, the model accurately captures the seasonal temperature progression observed in WOD data for both surface and subsurface layers (Fig S2 and Fig S3). However, the model also exhibits some discrepancies compared to WOD observations, such as an overestimation of temperature by 1°C to 2°C at depth in the AG during summer and in the 100-200m layer in all seasons in the SOO. This disparity may partially stem from the fact that the model and observations cover slightly different time periods, with most WOD observations in the region collected in the period 1960-1995. While the variability range in both WOD and the model is similar in both seas, model tends to underestimate salinity in high-salinity (>39 psu) waters in the AG by up to 1 psu (see Fig S2). Similarly, the model underestimates WOD salinity in the SOO at depth (200-300m) by approximately 0.5 psu (Fig S3). However, the sparse observational coverage of WOD in the region, particularly for salinity where most available observations are extracted from a few individual years, implies that the WOD observations may not necessarily be representative of the long-term

climatological conditions in the region (Fig S4). This is particularly pertinent given the strong seasonal and interannual variability characterizing temperature and salinity in the region, as demonstrated by the model simulations (see Fig 1).

The volume and seasonality of the Gulf's outflow via the Strait of Hormuz constitute an important parameter in our study. Johns et al. (2003) deployed acoustic Doppler current profiler (ADCP) moorings to measure the outflow's intensity and seasonal variations across the Strait of Hormuz between December 1996 to March 1998. The study identified a consistent and robust deep outflow below 45 meters, averaging 0.15 $\pm$ 0.03 Sv (where 1 Sv = 1 million cubic meters per second), fluctuating from 0.08 Sv in December to 0.18 Sv in March. Additionally, a more variable and weaker surface outflow of 0.06 $\pm$ 0.02 Sv was recorded above 45 meters. Our model simulates an annual deep outflow of 0.11 $\pm$ 0.06 Sv, ranging from 0.04 Sv in October to 0.15 Sv in March, and a surface outflow of 0.03 $\pm$ 0.02 Sv. The modeled annual outflow of 0.14 $\pm$ 0.07 Sv remains in agreement with Johns et al. (2003) estimate of 0.21 $\pm$ 0.05 Sv. Our model's results also align with prior estimates from indirect measurements and other model simulations (Table S2). In summary, despite some discrepancies, our model successfully captures the essential hydrographic features of the Arabian Gulf and Strait of Hormuz based on available data.

The evaluation of the model's ability to represent biological productivity is hindered by the lack of in-situ measurements of primary production and Chl-a pigment in the Gulf region. To address this, we compare our model's simulated chlorophyll-a levels to in-situ observations collected in the Qatar exclusive economic zone during six research cruises conducted between April 2015 and September 2016 (Al-Naimi et al., 2017). Our

comparison shows a good agreement in surface chlorophyll concentration throughout the year, both in terms of annual average and seasonality (Fig S5). The model also accurately reproduces the depth and magnitude of the deep chlorophyll maximum (DCM) in spring and summer but underestimates it in winter and overestimates it in autumn (Fig S5). Additionally, satellite chlorophyll data from the Ocean Color Climate Change Initiative (OC-CCI) exhibit a significant correlation with in-situ observations in the region, despite a systematic overestimation of the latter (Figure 1, Al-Naimi et al., 2017). This overestimation is likely due to the high turbidity of Gulf waters and the presence of suspended sediments, which affect the reliability of satellite-derived chlorophyll estimates. Nevertheless, the strong correlation ($r = 0.795$, $p < 0.001$) between in-situ and satellite data suggests that remotely sensed chlorophyll observations can effectively characterize Gulf biological productivity seasonality (Al-Naimi et al., 2017). To further evaluate our model, we compare simulated net primary productivity (NPP) seasonal anomalies with data-based NPP estimates from the vertically generalized production model (VGPM) by Behrenfeld and Falkowski (1997) (Fig S6). This comparison demonstrates good agreement between the model and data-based NPP estimates across the Gulf, particularly in winter and summer seasons, highlighting the consistency of simulated NPP variability with satellite-based observations (Fig S6).

Observations of oxygen levels in the Gulf are scarce. In this study, we compare the model's simulated oxygen with data from an extensive survey conducted in the Iran exclusive economic zone (EEZ) from summer 2018 to autumn 2019 (Saleh et al., 2021). The comparison, illustrated in Figure S7, indicates that the model effectively captures the

seasonal progression of low oxygen and bottom hypoxia, as indicated by the observations of Saleh et al. (2021). Specifically, oxygen levels were consistently lowest in late summer and early autumn (September) below 50 meters, while highest near the surface in May, both in the model and in the observations (Figure S7). Additionally, we compare key carbonate system parameters—DIC, TA, pCO_2, and pH—between the model and recent observations collected in December 2018 and May 2019 in the EEZ of Qatar by Izumi et al. (2022). With the exception of stations 1C and 2C, which are in close proximity to the coast and have shallow bathymetry not accurately represented in our model, DIC and TA exhibit good agreement with the collected data for both cruises (Fig S7). The model also shows good agreement with estimates of pCO_2 and pH for May 2019, but displays slightly larger discrepancies with respect to estimates from the December 2018 cruise. Nevertheless, the model reproduces the large-scale patterns of temporal and spatial variability observed in both variables. For instance, the higher pCO_2 levels observed in nearshore stations (1C, 2C, 3C) relative to those sampled farther offshore (4C, 5C, 6C, 6B) during May 2019, and the reverse pattern observed during December 2018, are both replicated in the model. Similarly, the lower pH recorded in nearshore stations compared to offshore stations in May 2019, and the opposite pattern observed in December 2018, are also reproduced in the model. In summary, our model's representation of biological production, oxygen levels, and the carbonate system aligns well with the available data, both in terms of the average range and the seasonal variability, as well as the large-scale spatial patterns.

Table S1. Trends under constant and varying climates. Trends (1980-2018) in AG-averaged sea surface temperature (in °C dec^{-1}), salinity (in psu dec^{-1}), density (in kg m^{-3} dec^{-1}), density gradient with the SOO (in kg m^{-3} dec^{-1}), Gulf outflow (in Sv dec^{-1}), transport of nitrogen through the Strait (in Gmol dec^{-1}), NPP (in g C m^{-2} yr^{-1} dec^{-1}), oxygen (in mmol m^{-3} dec^{-1}) and pH (in pH unit dec^{-1}) as simulated in the control HR and the constant climate (CC) simulations.

Simulation	Month	Temperature	Salinity	Density	Density gradient	Outflow	Transport of nitrogen	NPP	Oxygen (bottom)	pH$^{\perp}$ (bottom)
Control	Jan	0.108	0.014	-0.02	0.042	0.004	0.758	3.244	-0.41	-0.014
	Feb	0.17	0.006	-0.041	0.032	0.003	0.324	3.366	-0.912	-0.015
	Mar	0.352	-0.007	-0.102	-0.01	0.003	-1.108	2.406	-3.136	-0.019
	Apr	0.347	-0.003	-0.104	-0.008	0.002	-0.89	1.903	-3.344	-0.019
	May	0.358	0.002	-0.113	-0.035	-0.001	-0.855	2.207	-3.672	-0.02
	Jun	0.321	0.035	-0.082	-0.075	0	-0.158	3.129	-3.61	-0.02
	Jul	0.278	0.055	-0.057	-0.078	-0.002	0.821	3.239	-4.095	-0.021
	Aug	0.338	0.048	-0.086	-0.092	-0.004	0.418	2.824	-5.144	-0.022
	Sep	0.298	0.058	-0.063	-0.056	-0.007	1.583	3.859	-5.824	-0.023
	Oct	0.24	0.05	-0.046	-0.015	-0.003	0.746	5.754	-2.333	-0.018
	Nov	0.19	0.04	-0.032	0.02	-0.001	0.723	1.255	-0.119	-0.014
	Dec	0.105	0.025	-0.012	0.034	0.006	0.696	6.763	0.031	-0.013
Constant Climate	Jan	< 5e-4	< 5e-4	< 5e-4	0.001	< 5e-4	-0.139	0.397	0.006	-0.015
	Feb	-0.002	0.001	0.001	0.005	< 5e-4	-0.404	0.271	0.002	-0.015
	Mar	< 5e-4	0.001	< 5e-4	0.003	< 5e-4	0.087	0.245	0.006	-0.016
	Apr	< 5e-4	< 5e-4	< 5e-4	0.001	< 5e-4	0.145	0.409	0.024	-0.016
	May	< 5e-4	< 5e-4	< 5e-4	0.002	-0.001	0.147	0.453	-0.032	-0.016
	Jun	< 5e-4	< 5e-4	< 5e-4	0.004	< 5e-4	-0.028	0.424	-0.075	-0.016
	Jul	< 5e-4	< 5e-4	< 5e-4	0.002	0.001	-0.371	0.399	0.001	-0.017
	Aug	< 5e-4	< 5e-4	< 5e-4	0.003	< 5e-4	0.116	0.406	0.04	-0.017
	Sep	< 5e-4	< 5e-4	< 5e-4	< 5e-4	< 5e-4	0.068	0.398	0.036	-0.016
	Oct	< 5e-4	< 5e-4	< 5e-4	0.001	< 5e-4	0.065	0.479	0.02	-0.016
	Nov	< 5e-4	< 5e-4	< 5e-4	0.003	< 5e-4	0.016	0.399	0.073	-0.015
	Dec	< 5e-4	< 5e-4	< 5e-4	-0.001	< 5e-4	0.073	0.359	0.014	-0.015

Table S2. Gulf outflow estimates. Gulf inflow and outflow through the Strait of Hormuz (in Sv) as simulated in this study and from previous observation- and model-based estimates. The outflow is also separately estimated for shallow (depth above 45 m) and a deeper (depth below 45 m) layers following the description given by (Johns et al., 2003).

Study	Inflow	Outflow (total)	Outflow (deep)	Outflow (shallow)	Seasonality (Peak time/Minimum t
This study	0.15 ± 0.07	0.14 ± 0.07 [0.03-0.27]	0.11 ± 0.06	0.03 ± 0.02	May/October
(Johns et al., 2003)†	0.23 ± 0.04	0.21 ± 0.05	0.15 ± 0.03 [0.08-0.18]	0.06 ± 0.02	March/Decembe
(Pous et al., 2004)‡		0.21 [0.18-0.24]	0.16 [0.12-0.16]	0.01 [0-0.01]	NA⋆
(Ahmad & Sultan, 1991)⊤	0.19	0.17			NA⋆
(Chao et al., 1992)⊥		[0.03-0.17]			March/August
(Kämpf & Sadrinasab, 2006)⊥		[0.11-0.17]			spring/autumn
(Yao & Johns, 2010)⊥		[0.06-0.18]	[0.07-0.15]		July/January

† based on ADCP mooring

‡ based on geostrophic velocity estimates

⊤ based on a freshwater volume budget

⊥ based on numerical simulations

+ weak seasonality in deep outflow

⋆ NA = not available

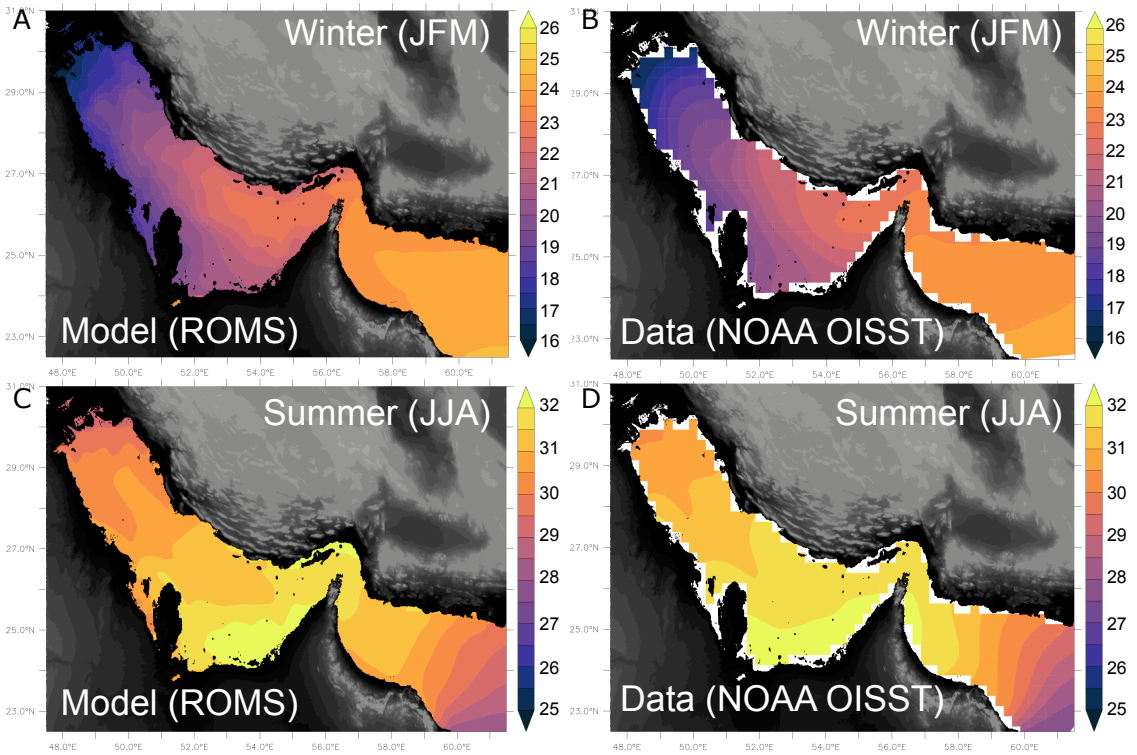

Figure S1. Evaluation of modeled sea surface temperature. Sea surface temperature as simulated (right) and from the NOAA Optimum Interpolation Sea Surface Temperature (OISST) data product (left) in winter (January-March, top panel) and summer (June-August, bottom panel).

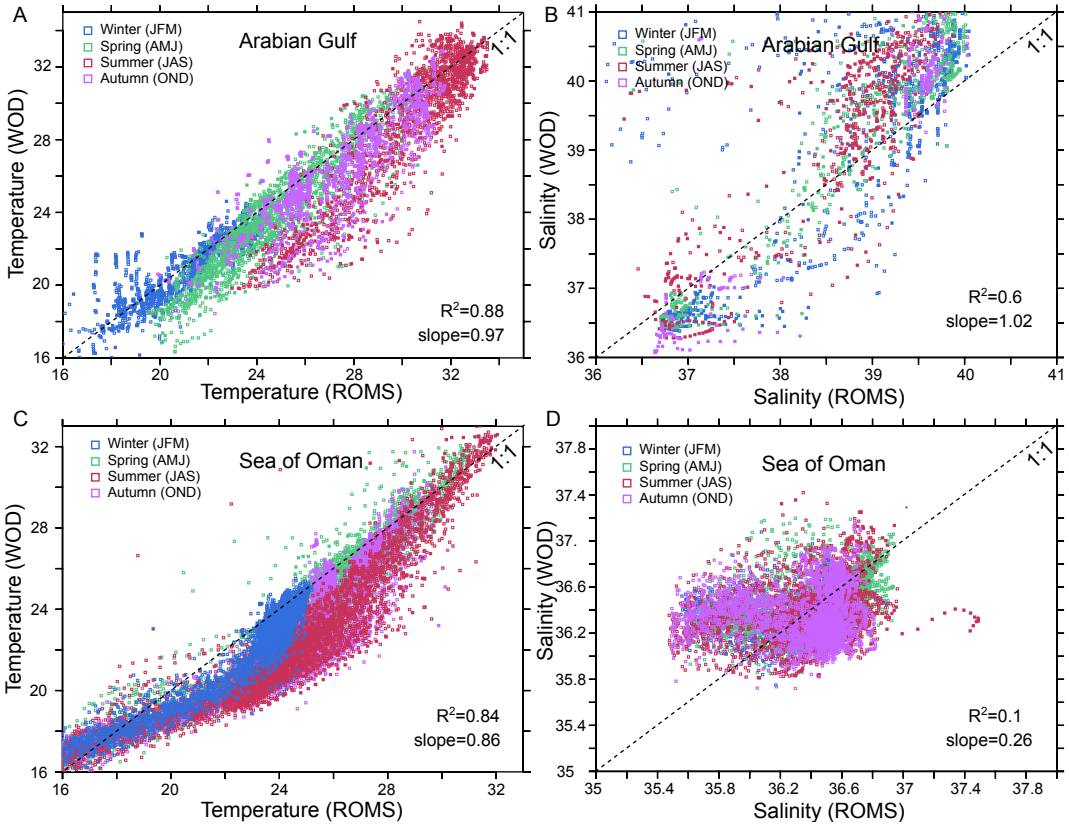

Figure S2. Comparison with WOD data for different seasons. Comparison between WOD observations and ROMS for temperature (left) and salinity (right) in the AG (top) and SOO (bottom) for different seasons.

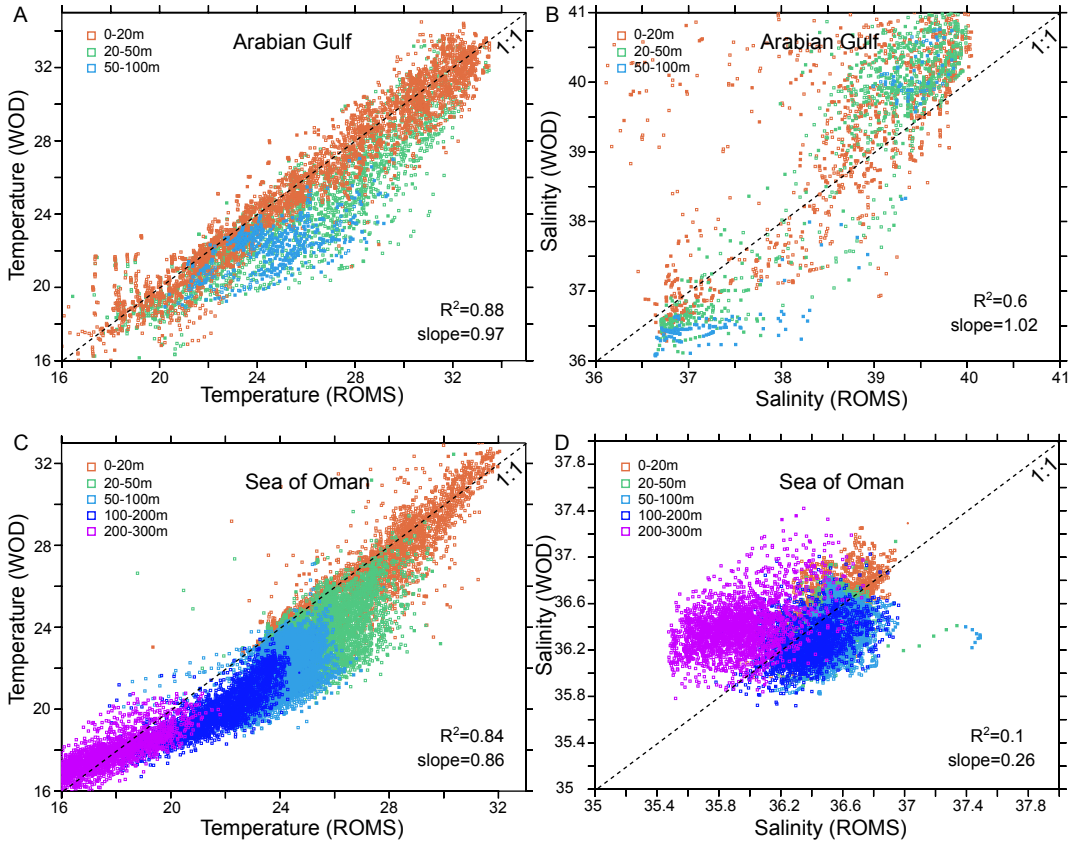

Figure S3. Comparison with WOD data for different vertical layers. Comparison between WOD observations and ROMS for temperature (left) and salinity (right) in the AG (top) and SOO (bottom) for different vertical layers.

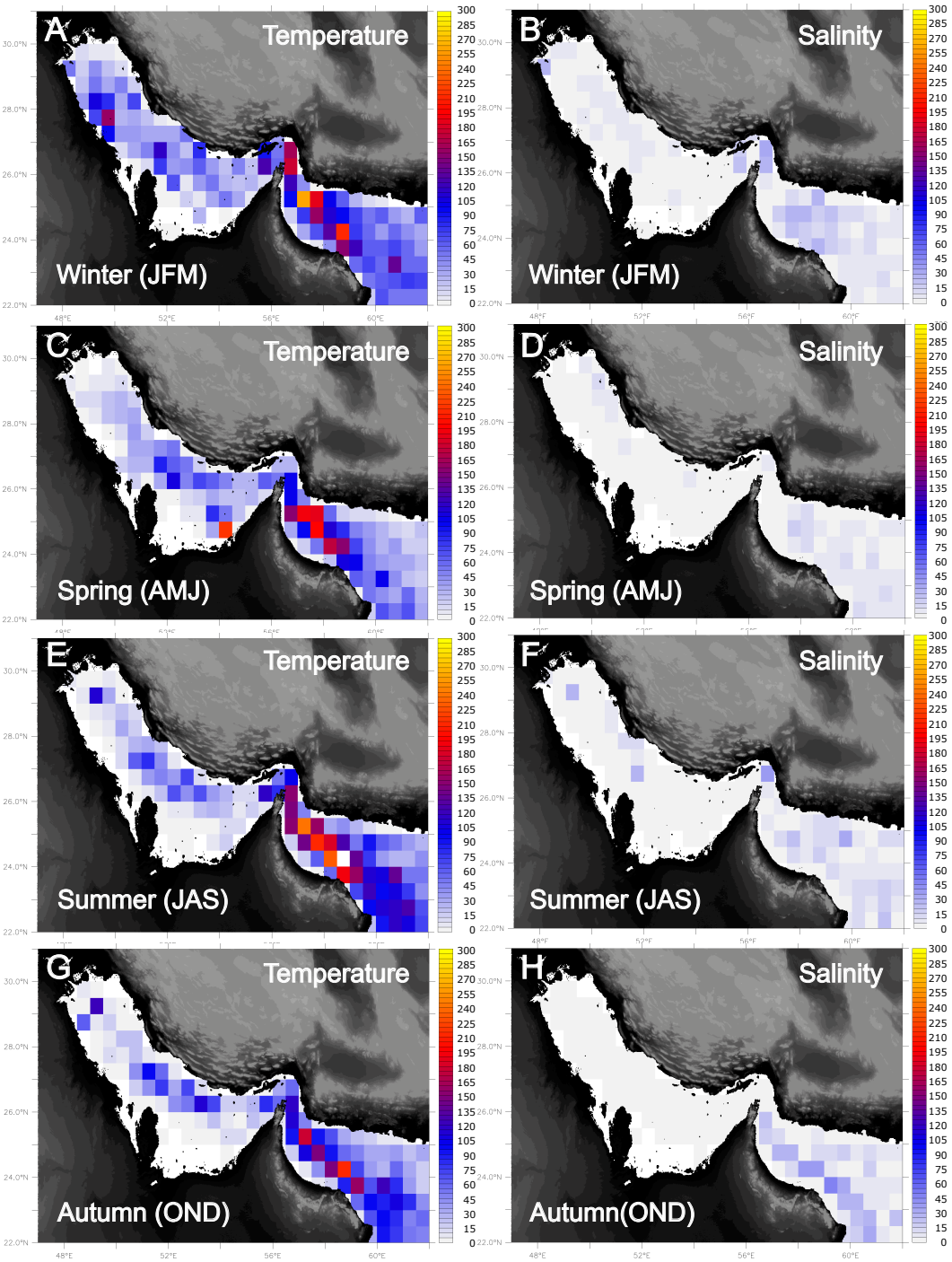

Figure S4. Number of observations. Number of available observed profiles in the World Ocean Database (2018) across the seasons in temperature (left) and salinity (right). Observations were binned on a monthly basis on a 0.5° x 0.5° regular grid. Model outputs were regridded on the same grid and sampled on observation grid points.

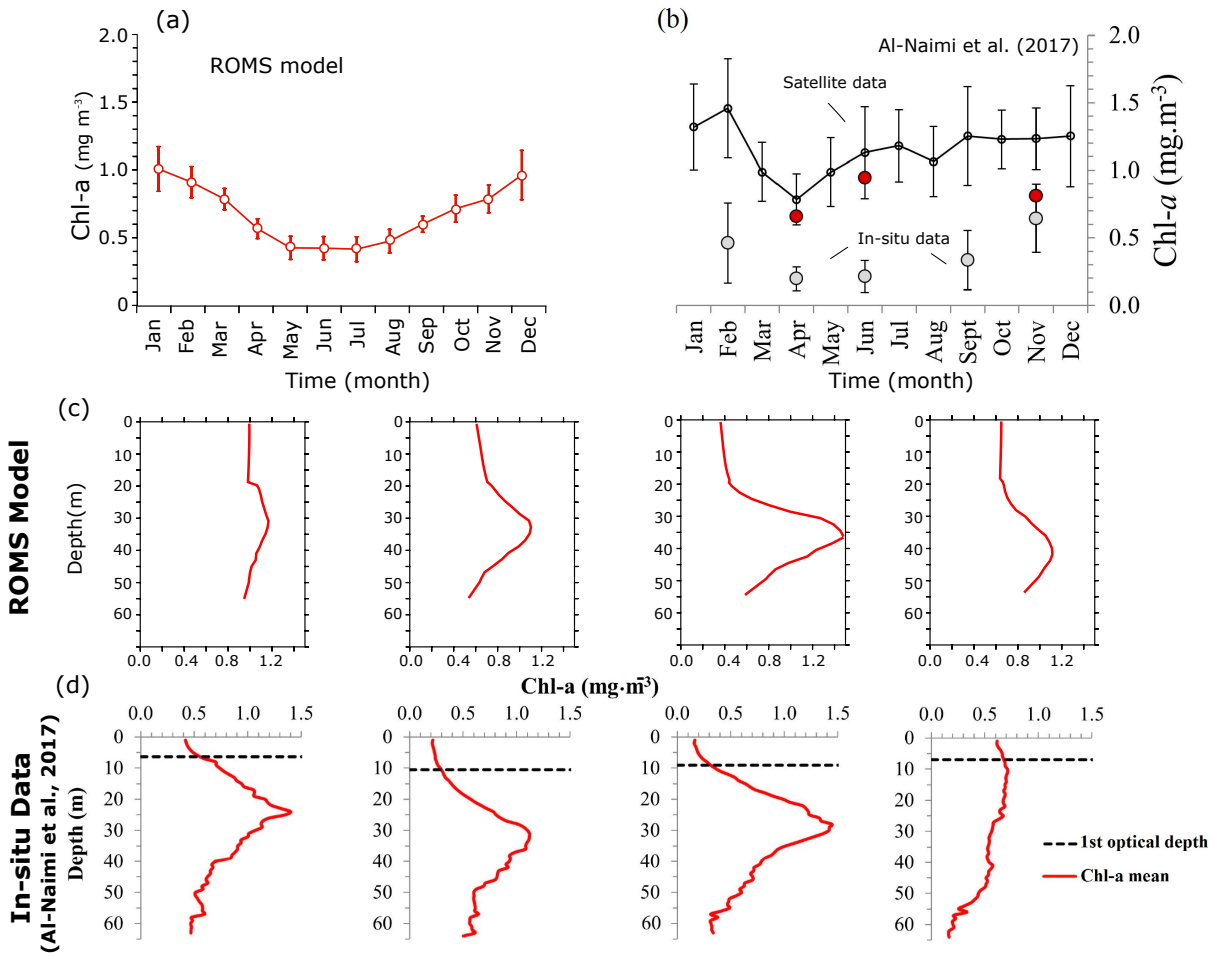

Figure S5. Evaluation of the model simulated chlorophyll-a concentrations. (a-b) Seasonal surface Chl-a concentrations (in mg m^{-3}) in the Qatar Exclusive Economic Zone (EEZ) (a) as simulated by ROMS and (b) from observations published by Al-Naimi et al. (2017). Gray circles show in-situ observations from six research cruises (2015-2016) while the black line indicates surface Chl-a based on the OC-CCI satellite monthly climatology (1997-2013). (c-d) Vertical profiles of Chl-a in the Qatar EEZ in winter (DJF), spring (MAM), summer (JJA) and autumn (SON) seasons as simulated by (c) ROMS and (d) from observations by Al-Naimi et al. (2017). Note that the seasonal in-situ chlorophyll profiles for winter, spring, summer and autumn are based on data collected in February 2016, April 2015/2016, June 2015, and September 2016/November 2015, respectively.

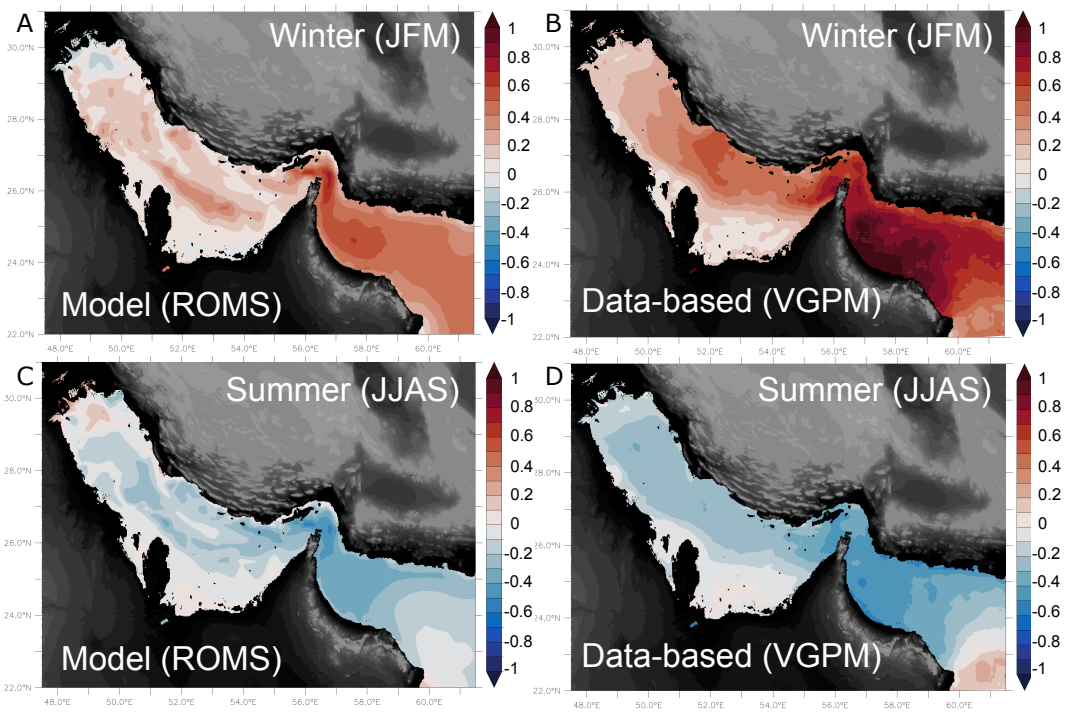

Figure S6. Evaluation of model simulated NPP seasonal variability. Seasonal anomalies in NPP (in g C m^{-2} yr^{-1}) in winter (top) and summer (bottom) as simulated by the model (left) and as estimated from satellite data based on the Vertically Generalized Production Model (VGPM) of Behrenfeld and Falkowski (1997) (right).

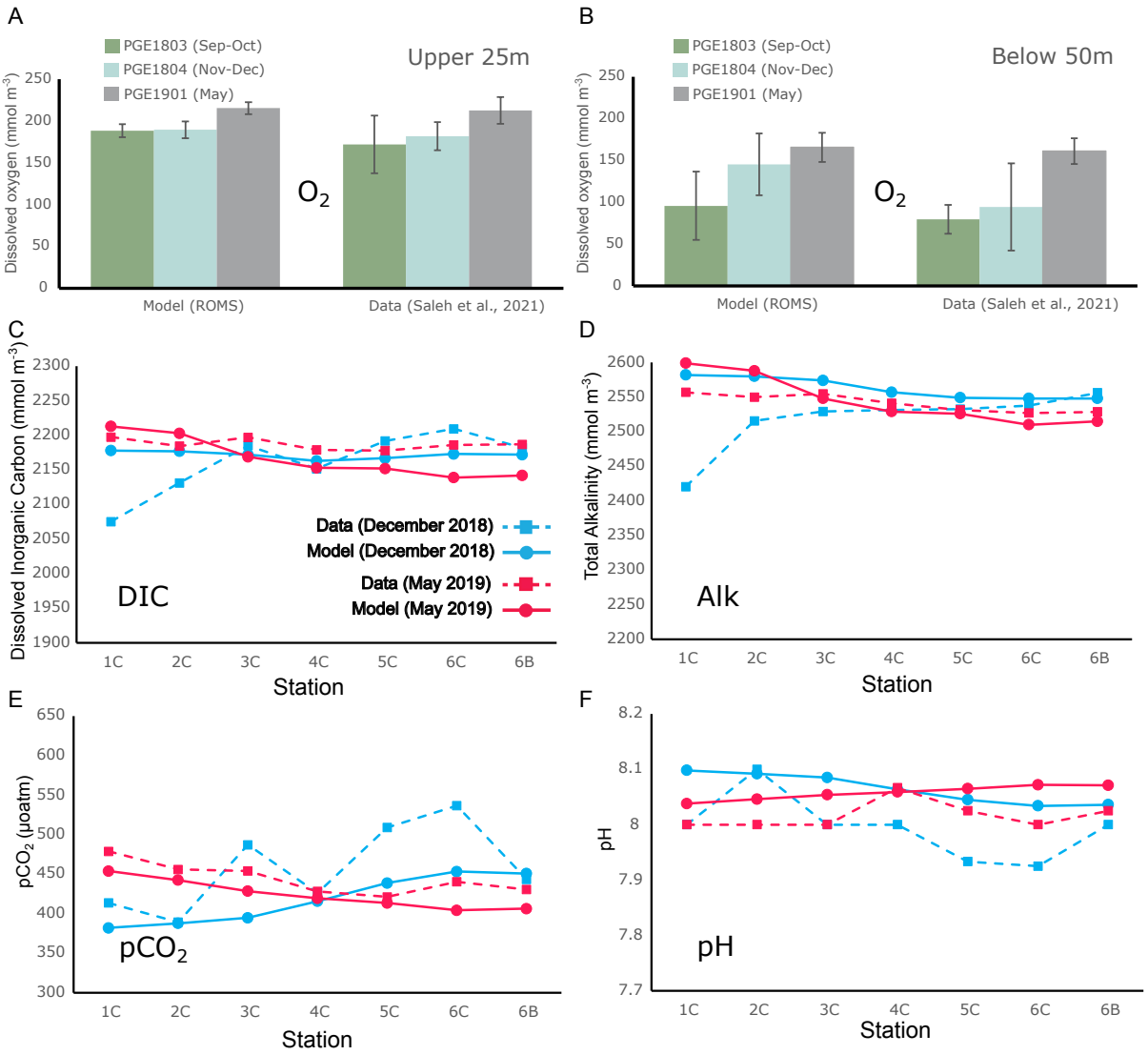

Figure S7. Comparison of simulated O_2 and carbon to available observations . (A-B) Comparison of the model simulated dissolved O_2 concentrations in the the AG (Iran EEZ) to observations collected during cruises PGE1803 (late summer), PGE1804 (late autumn), PGE1901, and PGE1902 (spring) in 2018 and 2019 by Saleh et al. (2021) in the upper 25m (A) and below 50m (B). Bar plots correspond to average concentrations for each cruise while error bars show standard deviations around the mean. (C-D) Comparison of the model simulated (C) DIC, (D) alkalinity, (E) pCO_2 and (F) pH to observations collected at seven stations in the Qatar EEZ in December 2018 and May 2019 (Izumi et al., 2022). For all comparisons, the model was sampled at the observation points.

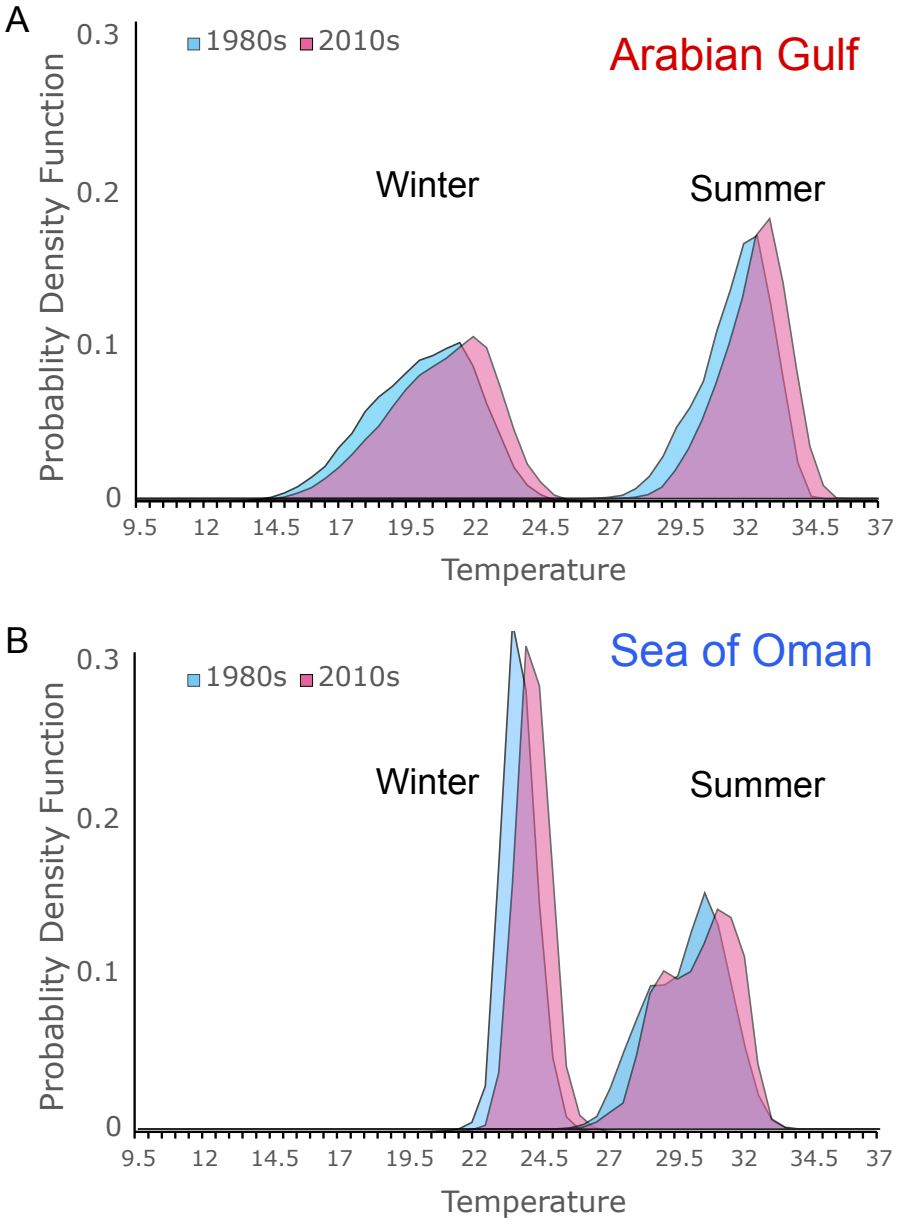

Figure S8. Change in temperature distributions in the AG and the SOO. Probability density function of simulated surface temperature during winter (JFM) and summer (JAS) in the 1980s (blue) and the 2010s (red) in the AG (top) and the SOO (bottom).

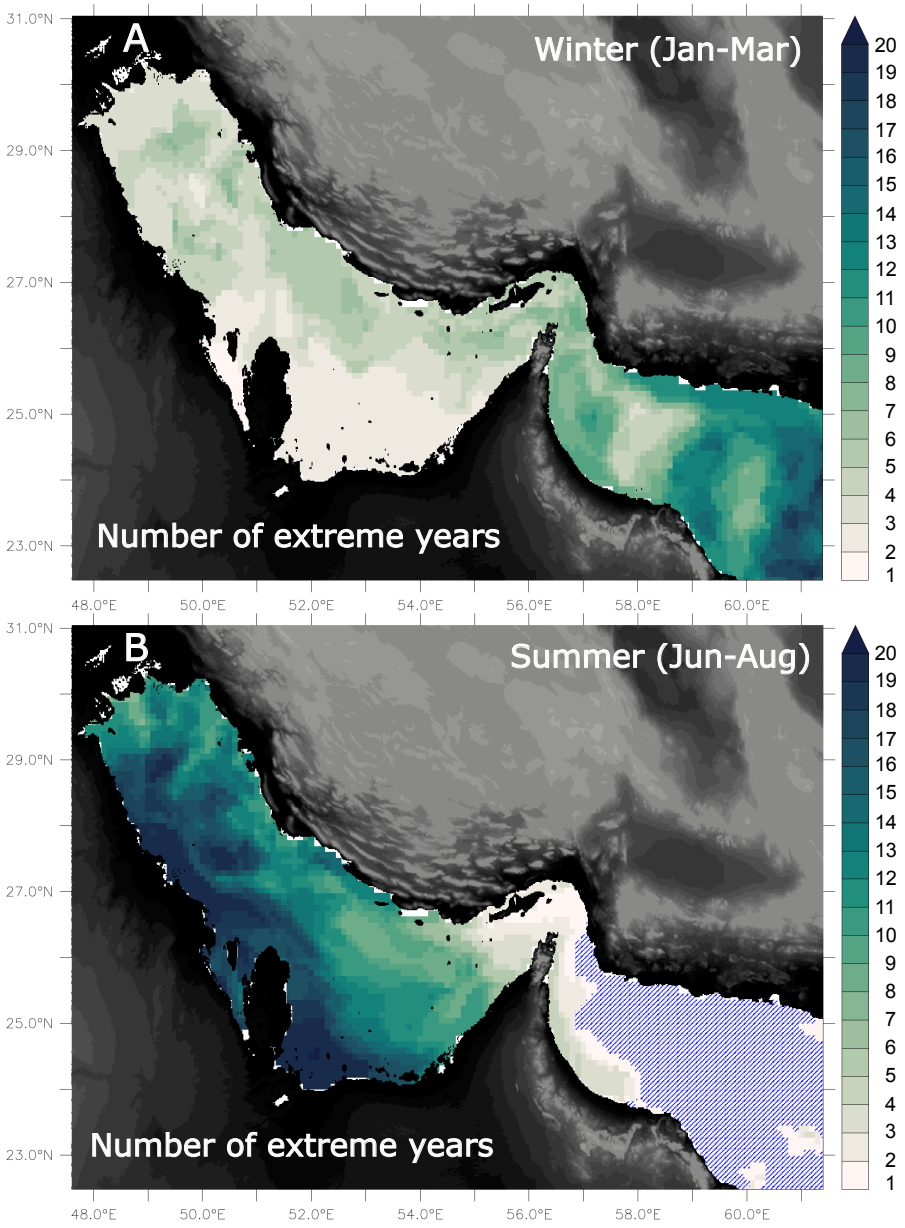

Figure S9. Number of extreme temperature years. Number of years where the average surface temperature for the season exceeds two standard deviations above the 1980s seasonal mean. (A) winter. (B) summer. Blue-hatching corresponds to areas where temperatures have not exceeded the defined threshold by the end of the study period.

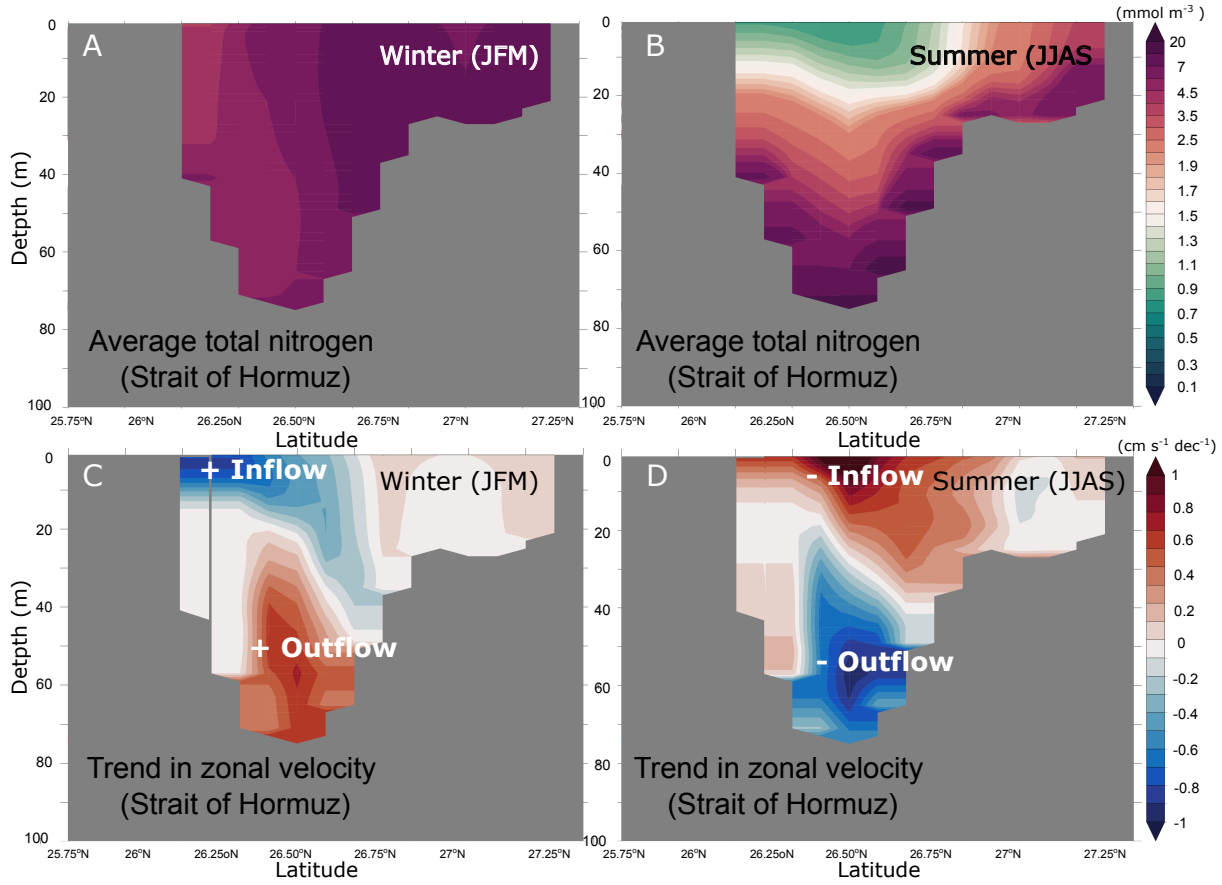

Figure S10. Nitrogen distribution and trends in zonal currents at the Strait. (A-B) vertical distribution of total nitrogen (in mmol m^{-3}) at Hormuz during winter (A) and summer (B). (C-D) Trends in zonal currents at Hormuz (in cm s^{-1} $decade^{-1}$) during winter (C) and summer (D). Positive values represent an increase of the Gulf outflow (or a decrease in the inflow).

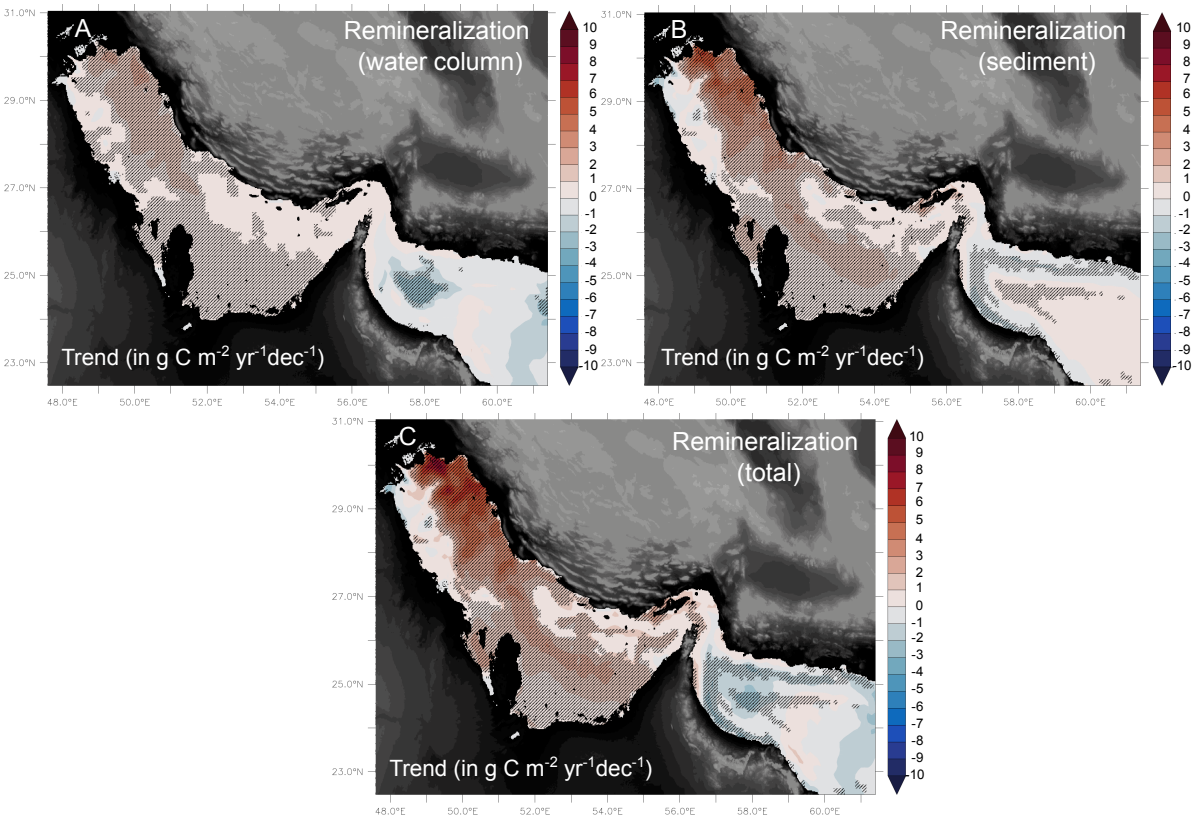

Figure S11. Changes in remineralization fluxes. Trends in remineralization fluxes (in g C m^{-2} yr^{-1} $decade^{-1}$) in the water-column (A), the sediment (B) and the total (water-column and sediment). Hatching indicates areas where trends are statistically significant at 95% confidence level.

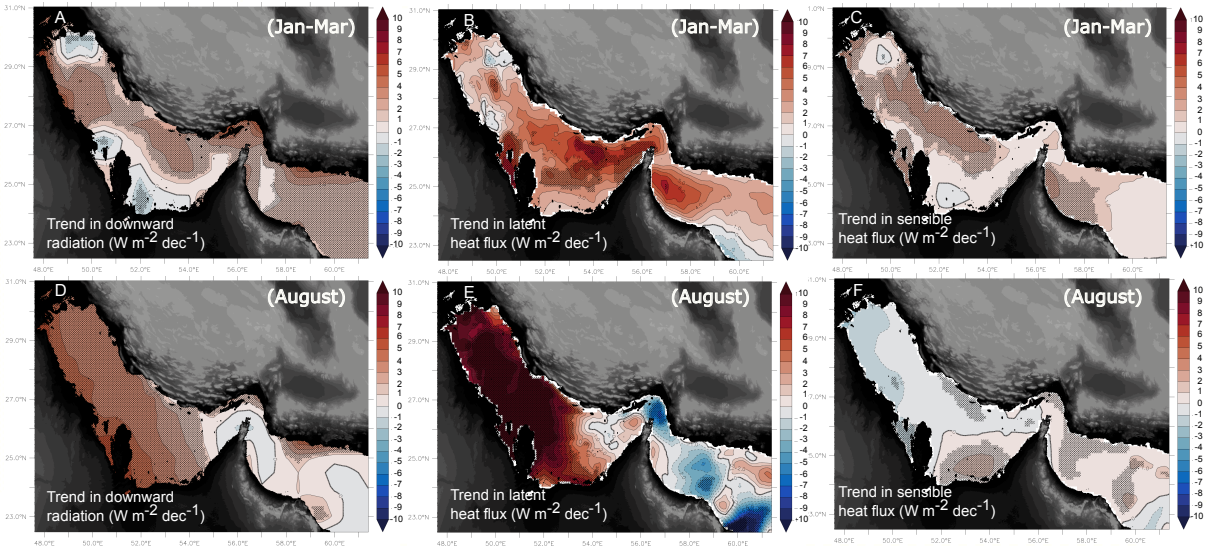

Figure S12. Drivers of AG warming. (A-C) Trends in downward radiation, latent and sensible heat fluxes (in W m^{-2} per decade) during winter months (JFM). (D-F) similar to (A-C) for the month of August. Hatching indicates areas where trends are statistically significant at 95% confidence level.

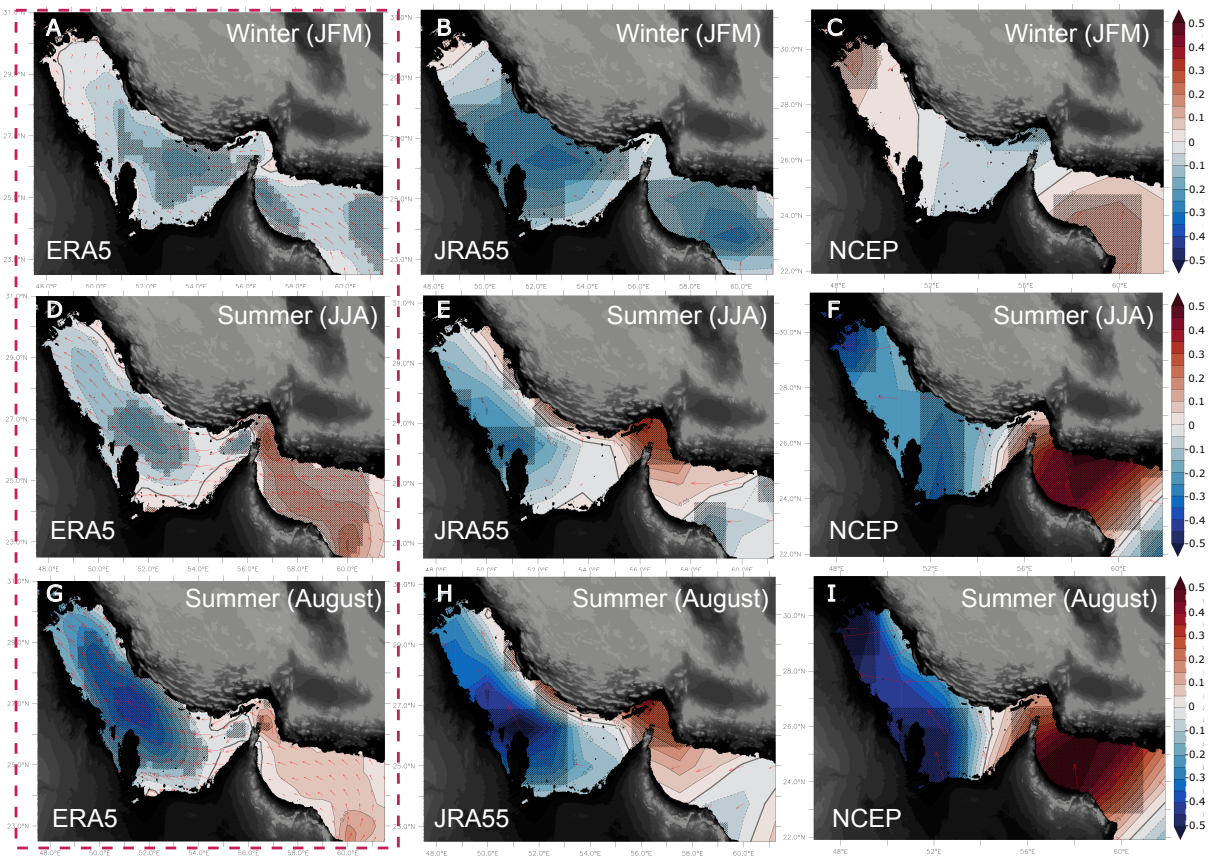

Figure S13. Changes in surface winds. Trends in surface winds in winter (A-C), summer (D-F) and for the month of August (G-I) based on ERA (left column), JRA55 (middle column) and NCEP (right column). Color shading indicates trends in wind speed (in m s^1 per decade), whereas arrows show trends in wind vector. Hatching indicates areas where trends are statistically significant at the 95% confidence level.

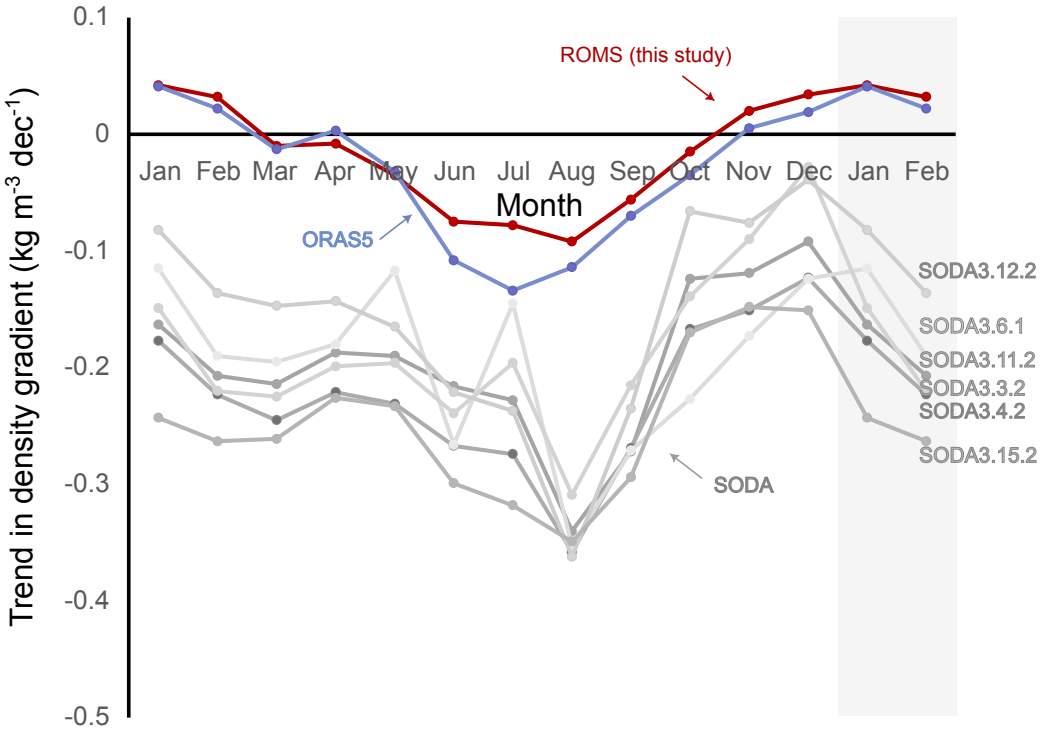

Figure S14. Changes in density gradient between the AG and the SOO based on different data products. Trends in density gradient between the AG and the SOO from ROMS (red), the ECMWF Ocean Reanalysis System 5 (ORAS5) reanalysis (blue) and different versions of Simple Ocean Data Assimilation (SODA) reanalyses (gray). The included SODA versions are: SODA3.3.2 (MERRA2), SODA3.4.2 (ERA-Interim), SODA3.6.1 (CORE2), SODA3.11.2 (DFS5.2), SODA3.12.2 (JRA55) and SODA3.15.2 (ERA5).

References

Ahmad, F., & Sultan, S. (1991). Annual mean surface heat fluxes in the arabian gulf and the net heat transport through the strait of hormuz. *Atmosphere-Ocean*, *29*(1), 54–61.

Al-Naimi, N., Raitsos, D. E., Ben-Hamadou, R., & Soliman, Y. (2017). Evaluation of satellite retrievals of chlorophyll-a in the arabian gulf. *Remote Sensing*, *9*(3), 301.

Al-Said, T., Naqvi, S., Al-Yamani, F., Goncharov, A., & Fernandes, L. (2018). Potential impact of human-induced physico-chemical changes in the arabian gulf on the oxygen minimum zone of the northwestern indian ocean. *Mar. Poll. Bull.*, *129*, 35–42.

Al-Yamani, F., & Naqvi, S. (2019). Chemical oceanography of the arabian gulf. *Deep Sea Research Part II: Topical Studies in Oceanography*, *161*, 72–80.

Behrenfeld, M. J., & Falkowski, P. G. (1997). Photosynthetic rates derived from satellite-based chlorophyll concentration. *Limnology and oceanography*, *42*(1), 1–20.

Chao, S.-Y., Kao, T. W., & Al-Hajri, K. R. (1992). A numerical investigation of circulation in the arabian gulf. *Journal of Geophysical Research: Oceans*, *97*(C7), 11219–11236.

de Verneil, A., Lachkar, Z., Smith, S., & Lévy, M. (2022). Evaluating the arabian sea as a regional source of atmospheric co 2: seasonal variability and drivers. *Biogeosciences*, *19*(3), 907–929.

Garcia, H., Boyer, T., Baranova, O., Locarnini, R., Mishonov, A., Grodsky, A. e., ... others (2019). World ocean atlas 2018: Product documentation. *A. Mishonov, Technical Editor*.

Griffies, S. M., Danabasoglu, G., Durack, P. J., Adcroft, A. J., Balaji, V., Boning, C. W., ... others (2016). Omip contribution to cmip6: experimental and diagnostic protocol for the physical component of the ocean model intercomparison project. *Geoscientific Model*

Development, 3231–3296.

Gruber, N., Clement, D., Carter, B. R., Feely, R. A., Van Heuven, S., Hoppema, M., ... others (2019). The oceanic sink for anthropogenic co2 from 1994 to 2007. *Science*, *363*(6432), 1193–1199.

Gruber, N., Frenzel, H., Doney, S. C., Marchesiello, P., McWilliams, J. C., Moisan, J. R., ... Stolzenbach, K. D. (2006). Eddy-resolving simulation of plankton ecosystem dynamics in the california current system. *Deep Sea Research Part I: Oceanographic Research Papers*, *53*(9), 1483–1516.

Izumi, C., Al-Thani, J. A., Yigiterhan, O., Al-Ansari, E. M. A., Vethamony, P., Sorino, C. F., ... Murray, J. W. (2022). Excess pco2 and carbonate system geochemistry in surface seawater of the exclusive economic zone of qatar (arabian gulf). *Marine Chemistry*, *247*, 104185.

Johns, W., Yao, F., Olson, D., Josey, S., Grist, J., & Smeed, D. (2003). Observations of seasonal exchange through the straits of hormuz and the inferred heat and freshwater budgets of the persian gulf. *Journal of Geophysical Research: Oceans*, *108*(C12).

Joos, F., & Spahni, R. (2008). Rates of change in natural and anthropogenic radiative forcing over the past 20,000 years. *Proceedings of the National Academy of Sciences*, *105*(5), 1425–1430.

Kämpf, J., & Sadrinasab, M. (2006). The circulation of the persian gulf: a numerical study. *Ocean Science*, *2*(1), 27–41.

Keeling, C. D., Piper, S. C., Bacastow, R. B., Wahlen, M., Whorf, T. P., Heimann, M., & Meijer, H. A. (2005). Atmospheric co2 and 13co2 exchange with the terrestrial biosphere and oceans from 1978 to 2000: observations and carbon cycle implications. In *A history of*

atmospheric co2 and its effects on plants, animals, and ecosystems (pp. 83–113). Springer.

Key, R. M., Kozyr, A., Sabine, C. L., Lee, K., Wanninkhof, R., Bullister, J. L., ... Peng, T.-H. (2004). A global ocean carbon climatology: Results from global data analysis project (glodap). *Global biogeochemical cycles*, *18*(4).

Krishna, M., Prasad, M., Rao, D., Viswanadham, R., Sarma, V., & Reddy, N. (2016). Export of dissolved inorganic nutrients to the northern indian ocean from the indian monsoonal rivers during discharge period. *Geochimica et Cosmochimica Acta*, *172*, 430–443.

Lachkar, Z. (2014). Effects of upwelling increase on ocean acidification in the california and canary current systems. *Geophysical Research Letters*, *41*(1), 90–95.

Lachkar, Z., & Gruber, N. (2013). Response of biological production and air–sea co2 fluxes to upwelling intensification in the california and canary current systems. *Journal of Marine Systems*, *109*, 149–160.

Lachkar, Z., Mehari, M., Al Azhar, M., Lévy, M., & Smith, S. (2021). Fast local warming is the main driver of recent deoxygenation in the northern arabian sea. *Biogeosciences*, *18*(20), 5831–5849.

Lachkar, Z., Smith, S., Lévy, M., & Pauluis, O. (2016). Eddies reduce denitrification and compress habitats in the arabian sea. *Geophysical Research Letters*, *43*(17), 9148–9156.

Large, W. G., McWilliams, J. C., & Doney, S. C. (1994). Oceanic vertical mixing: A review and a model with a nonlocal boundary layer parameterization. *Reviews of Geophysics*, *32*(4), 363–403.

Lauvset, S. K., Key, R. M., Olsen, A., Van Heuven, S., Velo, A., Lin, X., ... others (2016). A new global interior ocean mapped climatology: The 1× 1 glodap version 2. *Earth System*

Science Data, *8*(2), 325–340.

Marchesiello, P., Debreu, L., & Couvelard, X. (2009). Spurious diapycnal mixing in terrain-following coordinate models: The problem and a solution. *Ocean Modelling*, *26*(3-4), 156–169.

Middelburg, J. J., Soetaert, K., Herman, P. M., & Heip, C. H. (1996). Denitrification in marine sediments: A model study. *Global Biogeochemical Cycles*, *10*(4), 661–673.

Olsen, A., Lange, N., Key, R. M., Tanhua, T., Álvarez, M., Becker, S., ... others (2019). Glodapv2. 2019–an update of glodapv2. *Earth System Science Data*, *11*(3), 1437–1461.

Orr, J. C., Fabry, V. J., Aumont, O., Bopp, L., Doney, S. C., Feely, R. A., ... others (2005). Anthropogenic ocean acidification over the twenty-first century and its impact on calcifying organisms. *Nature*, *437*(7059), 681–686.

Pous, S., Carton, X., & Lazure, P. (2004). Hydrology and circulation in the strait of hormuz and the gulf of oman—results from the gogp99 experiment: 1. strait of hormuz. *Journal of Geophysical Research: Oceans*, *109*(C12).

Quigg, A., Al-Ansi, M., Al Din, N. N., Wei, C.-L., Nunnally, C. C., Al-Ansari, I. S., ... others (2013). Phytoplankton along the coastal shelf of an oligotrophic hypersaline environment in a semi-enclosed marginal sea: Qatar (arabian gulf). *Continental Shelf Research*, *60*, 1–16.

Ramesh, R., Purvaja, G., & Subramanian, V. (1995). Carbon and phosphorus transport by the major indian rivers. *Journal of Biogeography*, 409–415.

Saleh, A., Abtahi, B., Mirzaei, N., Chen, C.-T. A., Ershadifar, H., Ghaemi, M., ... Abedi, E. (2021). Hypoxia in the persian gulf and the strait of hormuz. *Marine Pollution Bulletin*, *167*, 112354.

Shchepetkin, A. F., & McWilliams, J. C. (2005). The regional oceanic modeling system (roms): a split-explicit, free-surface, topography-following-coordinate oceanic model. *Ocean modelling*, *9*(4), 347–404.

Wanninkhof, R. (1992). Relationship between wind speed and gas exchange over the ocean. *Journal of Geophysical Research: Oceans*, *97*(C5), 7373–7382.

Yao, F., & Johns, W. E. (2010). A hycom modeling study of the persian gulf: 2. formation and export of persian gulf water. *Journal of Geophysical Research: Oceans*, *115*(C11).

Zuo, H., Balmaseda, M. A., Tietsche, S., Mogensen, K., & Mayer, M. (2019). The ecmwf operational ensemble reanalysis–analysis system for ocean and sea ice: a description of the system and assessment. *Ocean science*, *15*(3), 779–808.